APPLICATION OF SPECTRAL POLARIMETRY TO A HAILSTORM AT LOW ELEVATION ANGLE

T.-Y. Yu[1,2,3,*], H. Le[1,2], Y. Wang[4,5], A. Ryzhkov[3,4,5], and M. Kumjian[6]

[1] School of Electrical and Computer Engineering, University of Oklahoma, Norman, OK, U.S.A.
[2] Advanced Radar Research Center, University of Oklahoma, Norman, OK, U.S.A.
[3] School of Meteorology, University of Oklahoma, Norman, OK, U.S.A.
[4] Cooperative Institute for Mesoscale Meteorological Studies, University of Oklahoma, Norman, OK, U.S.A.
[5] NOAA/OAR National Severe Storms Laboratory, NOAA, Norman, OK, U.S.A.
[6] Advanced Study Program, National Center for Atmospheric Research

Abstract

Polarimetric radar has proven to be an effective instrument to improve rainfall estimation, to enhance data quality, and to classify different types of hydrometeors. These measurements contain important dynamical and microphysical information of hydrometeors integrated over radar resolution volume. Moreover, spectral polarimetry was developed to unveil the polarimetric variables as a function of Doppler velocity within the resolution volume by combining Doppler and polarimetric measurements simultaneously. This provides a unique opportunity to study the hydrometeors microphysical properties in relation to the dynamics of the environment. The past study of spectral polarimetry has focused on using measurements from higher elevation angles, where both the size sorting from the hydrometeors' terminal velocities and the polarimetric characteristics are maintained. In this work, spectral polarimetry is applied to data from the lowest elevation angles, where polarimetric properties are maximized. An interesting feature was observed in polarimetric spectra from a hailstorm. A hypothesis of shear-induced size sorting is proposed and the theory for such process is derived.

The hypothesis is first supported by observations of a hailstorm on 24 April 2011 from the C-band OU-PRIME (Polarimetric Radar for Innovations in Meteorology and Engineering). By analyzing the polarimetric data from OU-PRIME, a mixture of rain and hail is suggested. This is further supported by the data collected by the closely located S-band KOUN radar, which is the upgraded polarimetric Weather Surveillance Radar-1988 Doppler (WSR-88D). A flexible numerical simulation is developed for this study, in which different types of hydrometeors such as rain, hail, snow, etc. can be considered individually or as a combination. Doppler spectra from both horizontal and vertical channels can be generated from given drop size distribution(s), wind shear, turbulence broadening, elevation angle, etc. The radar cross section from each hydrometeor is obtained from T-matrix approximation. The hypothesis is further verified using simulations. Furthermore, the impact of size sorting due to vertical shear is investigated and demonstrated using this simulation for various scenarios.

* *Corresponding author address:* Tian-You Yu, University of Oklahoma, Advanced Radar Research Center, 120 David L. Boren Blvd., Rm 4616, Norman, OK 73072; e-mail: tyu@ou.edu

1. RADAR OBSERVATIONS OF HAILSTORM

From NOAA, 40 hailstorm events were reported over Oklahoma starting at 6:04 UTC in Jefferson (lat: 34.17^o; lon: -98^o) on 24 April 2011 and ending at 4:09 UTC in Tulsa (lat: 36.3^o; lon: -95.99) on 25 April 201. A total of 19 counties was affected by hails with size ranging from 1.9 to 7.0 cm. Total property damage is approximately $65k. One of the hailstorms on 24 April 2011 in Oklahoma was observed simultaneously by both OU-PRIME and KOUN radars. At 18:50 UTC 24 April 2011, a hailstorm was crossing through Rush Spring (lat: 34.78; lon: -97.96) and ACME (lat: 34.77; lon: -97.92). In both these areas, hails were reported with size of 1.9 cm. The C-band OU-PRIME was operating with alternating PPI and RHI scans between 17:00:13 UTC and 19:59:49 UTC and the S-band KOUN radar was operating with Volume Coverage Pattern (VCP) 12. The scanning pattern for OU-PRIME and KOUN for a selected period is shown in Table 1.

Table 1: A summary of data collection from OU-PRIME and KOUN for a selected period of 18:47:29 UTC - 19:04:48 UTC on 24 April 2011

Time (UTC)	OU – PRIME	KOUN
18:47:29		VCP 12
18:47:50	PPI	
18:49:37	RHI	
18:50:09	PPI	
18:51:48		VCP 12
18:52:39	RHI	
18:53:31	PPI	
18:55:15	RHI	
18:56:07	PPI	VCP 12
18:58:21	RHI	
18:59:12	PPI	
19:00:29		VCP 12
19:00:58	RHI	
19:01:51	PPI	
19:04:02	RHI	
19:04:48		VCP12

In the PPI mode of OU-PRIME, total 8 elevation angles were used with a pulse repetition time (PRT) of 0.8475 ms. The update time of volume scan is approximately 2 - 3 min. In the RHI mode, OU-PRIME scan from 0^o to 20^o elevation angle in approximately 5.2 s with the same PRT of 0.8475 ms. The maximum unambiguous range of both RHI and PPI scan is 127 km. The S-band KOUN is located at 6.7842 km from OU-PRIME with azimuth of 156.9974^o. Moreover, VCP 12 was used for the KOUN for the time period. In this work, the storm of interest is located within the range of less than 60 km from OU-PRIME and both radars provide high-resolution polarimetric measurements. Although the scanning strategies and resolution are not the same for the two radars, valuable information can be obtained by the simultaneous observations from the two different radar wavelengths. For example, Borowska et al. (2011) studied hailstorm using reflectivity, differential reflectivity from the two radars. It is concluded that the understanding of hydrometeor characteristics within hailstorms is improved using simultaneous dual-wavelength observations. Picca and Ryzhkov (2012) collected data from OU-PRIME and KOUN also for a comparative analysis of hailstorm.

1.1. Dual-wavelength observations

$\hat{Z}_H$, $\hat{Z}_{DR}$, and $\hat{\rho}_{HV}$ from OU-PRIME's RHI scan at 18:58:21 UTC are shown in the left column of Fig. 1 from top to bottom. For better comparison, data from KOUN volume scan at 18:56:07 UTC were interpolated using nearest neighborhood to the same locations in the OU-PRIME's RHI scan and are shown in the right column. Additionally, $\hat{V}$, $\hat{\sigma}_v$ and $\hat{\phi}_{DP}$ from the same OU-PRIME RHI scan at 18:58:21 UTC are shown in the left column of Fig. 2, while results of hydrometeor classification algorithm (HCA) (Park et al., 2009), $\hat{\sigma}_v$ and $\hat{\phi}_{DP}$ interpolated from KOUN data are presented in the right column. Note that HCA was first implemented on KOUN volumetric data and subsequently interpolated to OU-PRIME's RHI coordinates. First of all, evident polarimetric signatures of hails in $\hat{Z}_H$ and $\hat{Z}_{DR}$ can be observed from both radars. A region of $\hat{Z}_H$ exceeding 60 dBZ can be observed at range of 48 - 52 km from OU-PRIME, which is considered as the core of the hailstorm. Thus, data from this selected storm will be analyzed. Similarly, high $\hat{Z}_H$ ($>$ 50 dBZ) can be observed from KOUN at similar locations. The $\hat{Z}_H$ and $\hat{Z}_{DR}$ of the hail core from OU-PRIME's RHI is characterized by a very high $\hat{Z}_H$ ($>$ 60 dBZ) and $\hat{Z}_{DR}$ ($>$ 4 dB). Moreover, $\hat{Z}_{DR}$ at OU-PRIME is 1 - 2 dB higher than the one at KOUN. This is likely caused by the resonance scattering at C band. The resonance effect is also responsible for the low $\hat{\rho}_{HV}$ (< 0.89) from OU-PRIME RHI comparing to higher $\hat{\rho}_{HV}$ (> 0.95) at KOUN (Borowska et al., 2011). In other words, the low $\hat{\rho}_{HV}$ at OU-PRIME values can be mixture of hydrometeors (e.g., rain and melting hail) in the radar resolution volume (Balakrishman and Zrnić, 1990; Tabary et al., 2010). Additionally, the $\hat{Z}_{DR}$ from OU-PRIME differential attenuation of as low as -3 dB behind hail core at ranges of approximately 54 $\sim$ 57 km while the $\hat{Z}_{DR}$ from KOUN is approximately 2 $\sim$ 3 dB at similar ranges (Borowska et al., 2011). This attenuation at C-band is possible a result from large raindrops and melting hails (Meischner et al., 1991; Ryzhkov et al., 2007; Anderson et al., 2011). Finally, from the interpolated HCA result at 18:56:07 UTC, it is evident that the mixture of hail and rain (HA) was identified by KOUN at around 50 - 55 km and at altitude between 1 and 4 km. The reason that a mixture of hail and rain is not directly identified at lower elevations is the time difference between the two observations.

The analysis of the observations from the two wavelengths strongly suggest the presence of a mixture of hail and rain in the lowest elevation of the OU-PRIME RHI scan near at range of approximately 50 $\sim$ 55 km at 18:58:21 UTC. However, radar signatures of hail need to be better understood in order to properly identify hail and estimate hail size. Spectral polarimetry has the potential to provide detailed information within the radar resolution volume. Therefore, spectral polarimetry was applied to OU-PRIME RHI data.

1.2. Signature of hail in spectral polarimetric variables at 0^o elevation angle

In Fig. 3, spectral reflectivity $\hat{S}_H$ (left column), spectral differential reflectivity $s\hat{Z}_{DR}$ (second column) are shown at selected ranges 49, 49.5, 50, 50.6 km (from top to bottom panel) at 0^o elevation angle 18:58:21 UTC. In the third column, the zoom-in OU-PRIME RHI reflectivity from range 45 $\sim$ 55 km and height up to 5 km at 18:58:21 UTC is shown on the top panel and the zoom-in of interpolated KOUN at 18:56:07 UTC is shown in the second. Additionally, the zoom-in of $\hat{Z}_{DR}$ from OU-PRIME and interpolated $\hat{Z}_{DR}$ from KOUN are shown in the third and fourth panels, respectively. The selected ranges for $\hat{S}_H$ and $s\hat{Z}_{DR}$ in the first two columns are denoted by arrows in four different colors in the third column. Horizontal axis for plot in the first two columns are radial velocity. The two selected ranges of 50 and 50.6 km can be considered as within the core of the hail storm. Note that both $\hat{S}_h$ and $s\hat{Z}_{DR}$ are manually dealiased to be within the interval of -24 to 10 ms^{-1} from the original interval of -17 to 17 ms^{-1}. Furthermore, horizontal dash blue lines in the $\hat{S}_h$ plots of left column indicated the spectral SNR threshold. The thicker lines of $\hat{S}_h$ and $s\hat{Z}_{DR}$ are the $\hat{S}_h$ and $s\hat{Z}_{DR}$ above the SNR threshold. The spectral SNR threshold is determined based on the work of Yu et al. (2012), given $R_1 = 0.04, R_2^2 = 0.5, R_3 = \frac{0.08}{100}, R_4^2 = \frac{0.2}{100}$ and $K = 30$. To quantify how the spectral differential reflectivity $s\hat{Z}_{DR}$ varies with radial velocity, a linear fitting was performed using only $s\hat{Z}_{DR}$ associated with the spectral SNR larger than the threshold (i.e., $s\hat{Z}_{DR}$ above the blue line). The fitted results are denoted by red lines in the $s\hat{Z}_{DR}$ plots. Additionally, values of $\hat{Z}_{DR}$ are also shown on the top of each $s\hat{Z}_{DR}$ subplot. It is interesting to point out that despite the same value of $\hat{Z}_{DR}$ = 5.9 dB is obtained at range 49 and

49.5 km, a negative and nearly zero slopes of $s\hat{Z}_{DR}$ are shown, which suggest different types of hydrometeor inside the two resolution volumes. Evidence of resonant scattering at shorter wavelength OU-PRIME can be easily observed with strong reflectivity and enhanced differential reflectivity at these gates. Moreover, a positive slope in $s\hat{Z}_{DR}$ is evident at 50.6 km. It is intriguing to investigate what cause the slope of $s\hat{Z}_{DR}$ to be different in these locations. In Fig. 4, spectral co-polar correlation coefficient $s\hat{\rho}_{HV}$, spectral differential phase $s\hat{\phi}_{DP}$ at the same selected ranges as those Fig. 3 are shown in the first and second column, respectively. However, zoom-in co-polar correlation coefficient from OU-PRIME RHI scan at 18:58:21 UTC and interpolated KOUN at 18:56:07 UTC are showed in the first and second panels from the top in the third column, respectively. In the lower next two plots, zoom-in differential phase from OU-PRIME RHI and zoom-in HCA from interpolated KOUN are presented. Note that the HCA results reveal heavy rain (HR) in these selected range at the lowest elevation. The time difference between the two measurements from OU-PRIME and KOUN needs to be emphasized. The selected time for spectra data and polarimetric variables is 18:58:21 UTC and the time for KOUN data is 18:56:07 UTC approximately, 2 minutes apart. In other words, the synthesized KOUN radial at 18:56:07 UTC only sample the edge of the storm core. Two minutes later, the storm core should have moved into the radial of 233.3^o according to the motion of the storm. If KOUN data would have been available at 18:58 UTC, it is speculated the mixture of rain-hail should have been obtained at these selected range.

It is clearly at 0^o elevation angle $\hat{S}_h$ are broaden, $s\hat{Z}_{DR}$ have slopes that change with range. Moreover, $s\hat{\rho}_{HV}$ and $s\hat{\phi}_{DP}$ seem to separate into two different parts of characteristics in some cases (i.e., range 49 km, 50.6 km). In other words, from $s\hat{\rho}_{HV}$ and $s\hat{\phi}_{DP}$, it can be hypothesized that these spectrum are resulted from two different types of hydrometeor. It has been reported that broad and flat-top spectra can be observed in strong shear environment (Yu et al., 2008). Broad spectrum can also be contribution from turbulence (Yanovsky et al., 2005). Moreover, from previous analysis from dual-wavelength observations, a mixture of rain and hail is likely to occur at these ranges. In summary, it is hypothesized that the $s\hat{Z}_{DR}$ slopes in 0^o elevation angle at these gates are caused by the shear-induced size sorting of a mixture of rain and hail in a turbulent environment. In the next chapter, hypothesis of these signatures will be verified using simulations.

2. SHEAR INDUCED SIZE SORTING AND SIMULATION

2.1. Review of shear-induced size sorting

It is known that a large drop has a larger terminal velocity than a smaller drop. This size sorting process is manifested by hydrometeor's terminal velocity. For radar observation with sufficiently high elevation angle, the difference of terminal velocity from hail and rain can produce well separated radial velocities. As a result, the contribution from hail and rain can be potentially distinguished in spectrum domain. Moreover, turbulence can broaden the spectra from rain and hail and can make the variation in differential reflectivity spectra flattened (e.g., Yanovsky, 2011). Spek et al. (2008) had shown that two types of ice particles mixed in the radar resolution volume can be separated and their individual DSDs can be retrieved using spectral polarimetry at higher elevation angle. Wang (2010) also demonstrated the separation in spectral components of rain and melting hail at the elevation angle of 45^o from the different hydrometeor's velocities.

Size sorting under wind shear was first recognized by Marshall (1953). The relation between wind shear and falling snow was observed and analyzed. Specifically, the trajectory of snow falling through a positive shear is considered as a parabola and the descent slope of the trajectory depends on the size of the snow. The canting angle of drop falling through a shear region was derived by Brussaard (1974, 1976), in which the effect of wind shear on drop's size-dependent falling velocity was obtained. Kumjian and Ryzhkov (2008) examined the kinematic mechanism of size sorting under sedimentation, updrafts, strong rotation and vertical wind shear. The magnitude of Z_{DR} can be used to indicate the severity of the storm. A good agreement between model and observation is shown for airflow patterns within severe storms through size sorting. In other words, falling hydrometeors with different size can land on different regions of the storms and therefore, different polarimetric signatures can be observed in these regions. Furthermore, in Kumjian and Ryzhkov (2012), it is shown that size sorting, caused by shear, can increase the Z_{DR} in pure rain for S-band radar. The high Z_{DR} is produced by the concentration of the large drops. In their work, simulation based on T-matrix was performed, where the mean and SD of canting angles are 0^o and 10^o, respectively.

In this work, spectral polarimetry is applied to observation of hailstorm at the low elevation angle. In this configuration, size-dependent terminal velocities resulted in almost the same radial velocities. However, in Sec. 1.2, interesting features in spectral polarimetric variables are observed. The results indicate the presence of size sorting. Therefore, it is hypothesize that the size sorting at such low elevation angle is mainly contributed by vertical shear. In this chapter, the theory of hydrometeor's velocity in a shear environment is presented. Moreover, a numerical simulation of spectral polarimetry in a shear and turbulent environment is developed. Simulation results are used to verify the hypothesis of producing observed signature in $s\hat{Z}_{DR}$ proposed in Chapter 5. The motion of hydrometeor falling in turbulence or shear environment is related to air flow. The approximate trajectory of a hydrometeor and its inclination are related to shear (Pinsky and Khain, 2006). Equation of motion for falling hydrometeor was derived in many previous studies, such as Brussaard (1974, 1976); Bohne (1982); Beard and Jameson (1983), etc. and is discussed now. The primary forces on a single hydrometeor are the gravity force and drag force. In this work, only horizontal ($\mathbf{a}_h$) and vertical ($\mathbf{a}_z$) direction are considered, in which $\mathbf{a}_z$ is upward. Let's consider a hydrometeor of size D and velocity $\mathbf{V} = \mathbf{a}_h V_h + \mathbf{a}_z V_z$ falling through a shear region. Initially, the hydrometeor is located at height H and its velocity is equal to the wind velocity at H, $\mathbf{U}(H) = \mathbf{a}_h U_h$, where only the horizontal air motion is considered.

From Newton's second law, the net force $\mathbf{F}_n$ on drop is represented in the following equation.

$$\mathbf{F}_n = \mathbf{F}_g + \mathbf{F}_d \tag{1}$$

where $\mathbf{F}_g = m\mathbf{g}$ is the gravity force and $\mathbf{g} = \mathbf{a}_h\, 0 + \mathbf{a}_z(-g)$ and g is the gravity. The drag (or air resistance) force $\mathbf{F}_d$ is obtained using the following equation (Bohne, 1982).

$$\mathbf{F}_d = -m\frac{\mathbf{V} - \mathbf{U}}{\tau} \tag{2}$$

where the time constant $\tau = \frac{V_t(D)}{g}$. After derivations, hydrometeor's horizontal and vertical velocities are obtained as shown in the following equations.

$$V_h(t) = U_h(t) - \frac{s\, V_t^2(D)}{g} \tag{3a}$$

$$V_z(t) = -\frac{s\, V_t^2(D)}{g} - V_t(D) \tag{3b}$$

where $V_t(D)$ is terminal velocity and $s = \frac{dU_h}{dz}$ is constant vertical shear. The radar observed velocity is the sum of the radial components from the two velocities. For higher legation, the size sorting can be contributed from both horizontal and vertical components of the falling hydrometeors. However, for low elevation angle of 0.5^o, the presence of size sorting is contributed mainly from the shear term in the horizontal component.

2.2. Description of simulations

In Spek et al. (2008), models of Doppler spectrum and differential reflectivity spectrum (i.e., sZ_{DR}) are developed for a mixture of two types of ice particles, each with its DSD, in a turbulent environment. Similar models are used in Wang (2010) for a mixture of rain and melting hail. However, neither of the two studies consider the shear-induced size sorting and at the low elevation angle. In this work, simulation of Doppler spectrum and differential reflectivity spectrum based on the work developed in Wang (2010). However, the size sorting derived in $(3a)$ and $(3b)$ is considered.

A simulation that considers the shear-induced size sorting mechanism is developed to model both Doppler spectra and differential reflectivity spectra for a mixture of hydrometeor's type in turbulence at C-band for any given elevation angle. The input parameters to the simulation include shear (s), elevation angle (θ), turbulence broadening (σ_b), melting ratio (f_w) and a range of sizes for rain (D_w) and for hail (D_h). The output of this simulation is Doppler spectrum for both polarizations ($S_H(v)$ and $S_V(v)$), and differential reflectivity spectrum ($sZ_{DR}(v)$) The basic idea is to generate Doppler spectrum from both H and V channels for a given hydrometeor type from shear-induced size sorting. Subsequently, the spectra is broadened by turbulence. The same procedure is repeated for the next hydrometeor type. The resulted Doppler spectra is the superposition of the broadened spectrum from all the types with the same polarization. Consequently, the differential reflectivity spectrum are obtained by the ratio of the two spectrum from H and V channels. In order to generate a Doppler spectra for a specific hydrometeor type, its DSD, radar backscattering cross sections for both H and V channels, the relation of velocity and size are needed. A detailed description of the simulation can be found in Le (2013).

After a series of attempts with different values of wind shear, turbulence and mixture of rain and hail. $s\hat{Z}_{DR}$ slopes from Fig. 3 of OU-PRIME's RHI scan are produced in Fig. 5. Specifically, a negative shear of ($s = -0.025$), turbulence ($\sigma_b = 1.5$) are applied to the mixture of large drops and melting hails with a melting ratio of 0.4. The negative $s\hat{Z}_{DR}$ slope shown in the top right panel is resulted from large drops of 5.2 $\sim$ 7 mm and fewer large melting hails (Λ = 0.7 in DSD) in range of 5.6 $\sim$ 25 mm. The highest value of $s\hat{Z}_{DR}$ of 6 dB at -18 ms^{-1} is dominant by large raindrops. On the other hand, the lower $s\hat{Z}_{DR}$ value of approximately 4 dB at 0 ms^{-1} is mainly contributed from hail. As a result, a negative slope in $s\hat{Z}_{DR}$ is obtained.

In the middle panel, $s\hat{Z}_{DR}$ with large value of 6 dB can be observed from the mixture of dominating rain and melting hail. As mentioned earlier, the zero slope of $s\hat{Z}_{DR}$ can be also resulted from non-shear and turbulent environment at lower elevation angle. For spectral polarimetry at higher elevation angle, $s\hat{Z}_{DR}$ slope is anticipated due to the size-sorting from the size-dependent terminal velocity. However, zero slope of $s\hat{Z}_{DR}$ can also be resulted from strong turbulent condition, in which the velocity of hydrometeors are well mixed.

The bottom right panel in Fig. 5 shows positive $s\hat{Z}_{DR}$ slope from the mixture. In this case, Λ = 0.4 is used for hail's DSD in order to produce higher $s\hat{Z}_{DR}$ (3.5 - 5.2 dB) from more number of large hails. In other words, the more number the large melting hails occurs, the higher the hail $s\hat{Z}_{DR}$ is. Moreover, rain has less contribution to the Doppler spectrum as shown in the bottom left panel with D_0 of 3.7 mm and N_o^w = 1000. The size of raindrops range from 0.08 to 7 mm in this case. A lower $s\hat{Z}_{DR}$ form raindrop is shown on the lower right panel. As a result, the positive slope of $s\hat{Z}_{DR}$ is mainly contributed from melting hail. However, a smaller amount of raindrops is needed to produce the low $s\hat{Z}_{DR}$ value on the left side of $s\hat{Z}_{DR}$ spectrum.

3. CONCLUSIONS

The goal of this work is to construct a polarimetric spectrum model to investigate hail signature appeared at the low elevation angle. The advantage of spectral polarimetric is to reveal polarimetric variables as a function of Doppler velocity within the radar resolution volume. Therefore, if the radial velocity depends on the size of hydrometeors, i.e., size sorting is present, then the polarimetric property of hydrometeor from these sizes can be derived. Considering a mixture of rain and melting hails falling through a shear and turbulence environment, the hydrometeors velocity as well as its canting angle are derived to be size dependent. The theory is subsequently applied to simulate Doppler and differential reflectivity spectra.

References

Anderson, M. E., L. D. Carey, W. A. Petersen, and K. R. Knupp, 2011: C-band dual-polarimetric radar signatures of hail. *National Weather Association, Electronic of Operational Meteorology*, **EJ02**.

Balakrishman, N., and D. S. Zrnić, 1990: Use of polarization to characterize precipitation and discriminate large hail. *J. Atmos. Sci.*, **47**, 1525–1540.

Beard, K. V., and A. R. Jameson, 1983: Raindrop canting. *J. Atmos. Sci.*, **40**(448-453).

Bohne, A. R., 1982: Radar detection of turbulence in precipitation environments. *J. Atmos. Sci.*, **39**, 1819–1837.

Borowska, L., A. V. Ryzhkov, and D. S. Zrnić, 2011: Attenuation and differential attneuation of 5-cm-wavelength radiation in melting hail. *J. Appl. Meteor. and Climatology*, **50**, 59–76.

Brussaard, G., 1974: Rain-induced cross polarization and raindrop canting. *Elec. Letters*, **10**, 411–412.

Brussaard, G., 1976: A meteorological model for rain-included cross polarization. *IEEE Trans. Antennas Propagat.*, **24**, 5–11.

Kumjian, M. R., and A. V. Ryzhkov, 2008: Microphysical size sorting revealed from dual-polarization doppler radar. *Extended Abstracts, 88^{88} Annual AMS Meeting, New Orleans, Amer. Meteor. Soc.*, **P2.13**.

Kumjian, M. R., and A. V. Ryzhkov, 2012: The impact of size sorting on the polarimetric radar variables. *J. Atmos. Sci.*, **69**, 2042–2060.

Le, H., 2013: *Application of Spectral Polarimetry to a Hailstorm at Low Elevation Angle Using C-band Polarimetric Radar*. Master's thesis, University of Oklahoma.

Marshall, J. A., 1953: Precipitation trajectories and patterns. *J. Meteor.*, **5**, 165–166.

Meischner, P. F., V. N. Bringi, D. Heimanm, and H. Holler, 1991: A squall line in southern germany: kinematics and precipitation formation as deduced by advanced polarimetric and doppler radar measurements. *Mon. Wea. Rev.*, **119**, 678–701.

Park, H., A. V. Ryzhkov, D. S. Zrnić, and K.-E. Kim, 2009: The hydrometeor classification algorithm for the polarimetric WSR-88D: Description and application to an MCS. *Wea. Forecasting*, **24**, 730–748.

Picca, J., and A. V. Ryzhkov, 2012: A dual-wavelength polarimetric analysis of the 16 May 2010 Oklahoma city extreme hailstorm. *Mon. Wea. Rev.*, **140**, 1385–1403.

Pinsky, M. B., and A. P. Khain, 2006: Initiation of drop velocity oscillations during their fall in a vertically sheared flow with embedded velocity fluctuation. *Geophysical and Astrophysical Fluid Dynamics*, **78**.

Ryzhkov, A. V., D. S. Zrnić, P. Zhang, J. Krause, H. S. Park, D. Hudak, J. Young, and J. L. Alford, 2007: Comparison of polarimetric algorithms for hydrometeor classification at s and c bands. *33rd Conference on Radar Meteorology, Caims, Queensland*, **Queensland**(5-10).

Spek, A. L. J., C. M. H. Unal, D. N. Moisseev, H. W. J. Russchenberg, V. Chandrasekar, and Y. Dufournet, 2008: New technique to categorize and retrieve the microphysical properties of ice particles above the melting layer using radar dual-polarization spectral analysis. *J. Atmos. Oceanic Technol.*, **25**, 482–497.

Tabary, P., C. Berthet, P. Dupuy, J. Figueras, B. Fradon, J. F. Georgis, R. Hogan, F. Kabeche, and J. P. Wasselin, 2010: Hail detection and quantification with c-band polarimetric radars: Results from a two-year objective comparison against hailpads in the south of france. *6th ERAD, Sibiu, Romania*, **6-10**.

Wang, Y., 2010: *The application of spectral analysis and artificial intelligence methods to weather radar*. Ph.D. thesis, University of Oklahoma.

Yanovsky, F. J., 2011: *Inferring microstructure and turbulence properties in rain through observations and simulations of signal spectra measured with Doppler-polarimetric radars*. pp. 501–542, Polarimetric Detection, Characterization, and Remote Sensing, NATO Science for Peace and Security Series C. Springer.

Yanovsky, F. J., H. W. J. Russchenberg, and C. M. H. Unal, 2005: Retrieval of information about turbulence in rain by using Doppler-polarimetric radar. *IEEE trans. Microwave Theory and Techniques*, **53**(2), 444–450.

Yu, T.-Y., R. R. Rondinels, and R. D. Palmer, 2008: Investigations of non-gaussian doppler spectra observed by weather radar in a tornadic supercell. *J. Atmos. Oceanic Technol.*, **26**, 444–461.

Yu, T.-Y., X. Xiao, and Y. Wang, 2012: Statistical quality of spectral polarimetric variables for weather radar. *J. Atmos. Oceanic Technol.*, **29**, 1221–1235.

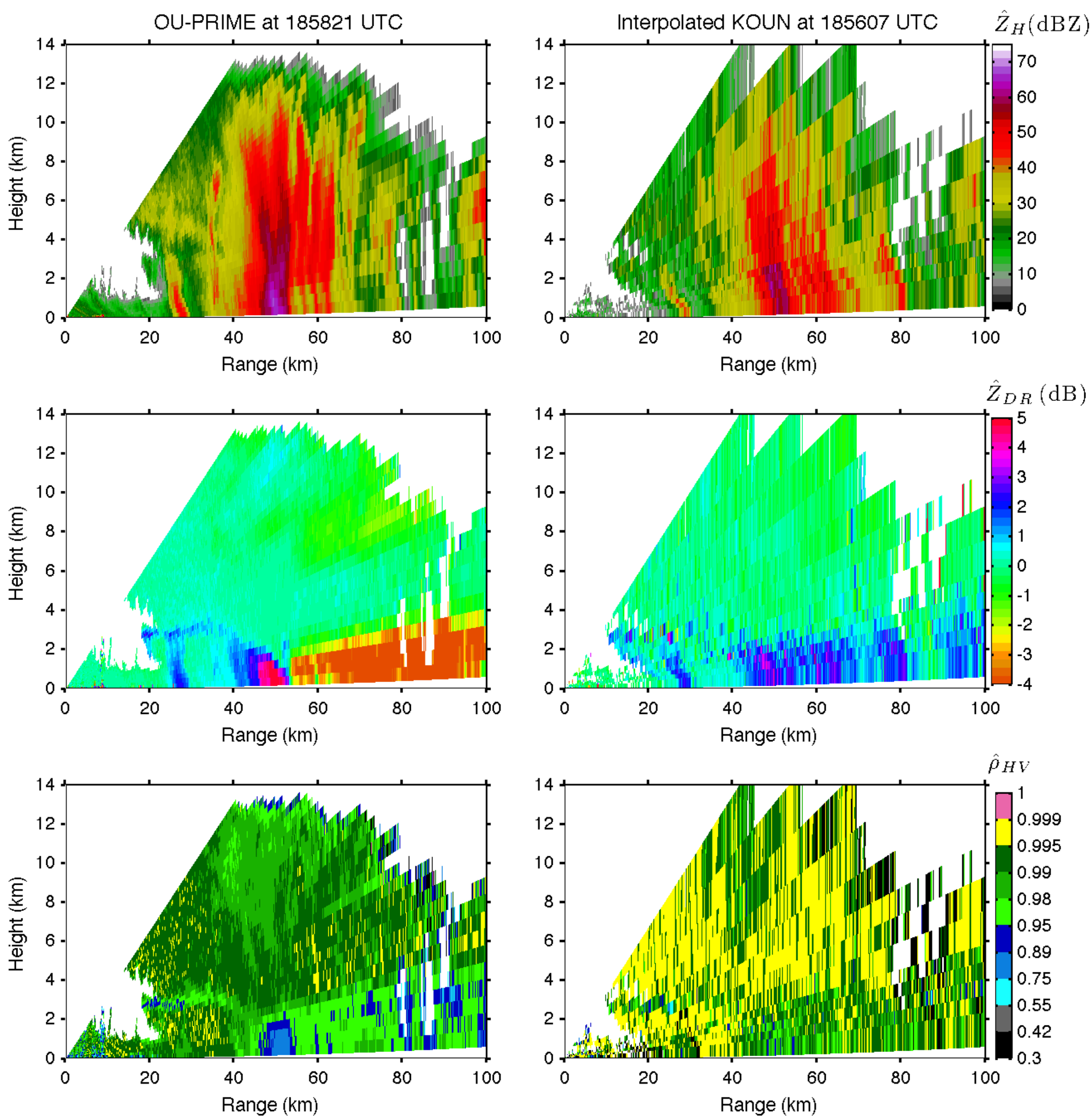

Figure 1: (Left) Reflectivity, differential reflectivity and co-polar correlation coefficient from the OU-PRIME RHI scan at 18:58:21 UTC. (Right) Reflectivity, differential reflectivity and co-polar correlation coefficient interpolated from the KOUN volume scan to OU-PRIME's RHI are presented at 18:56:07 UTC.

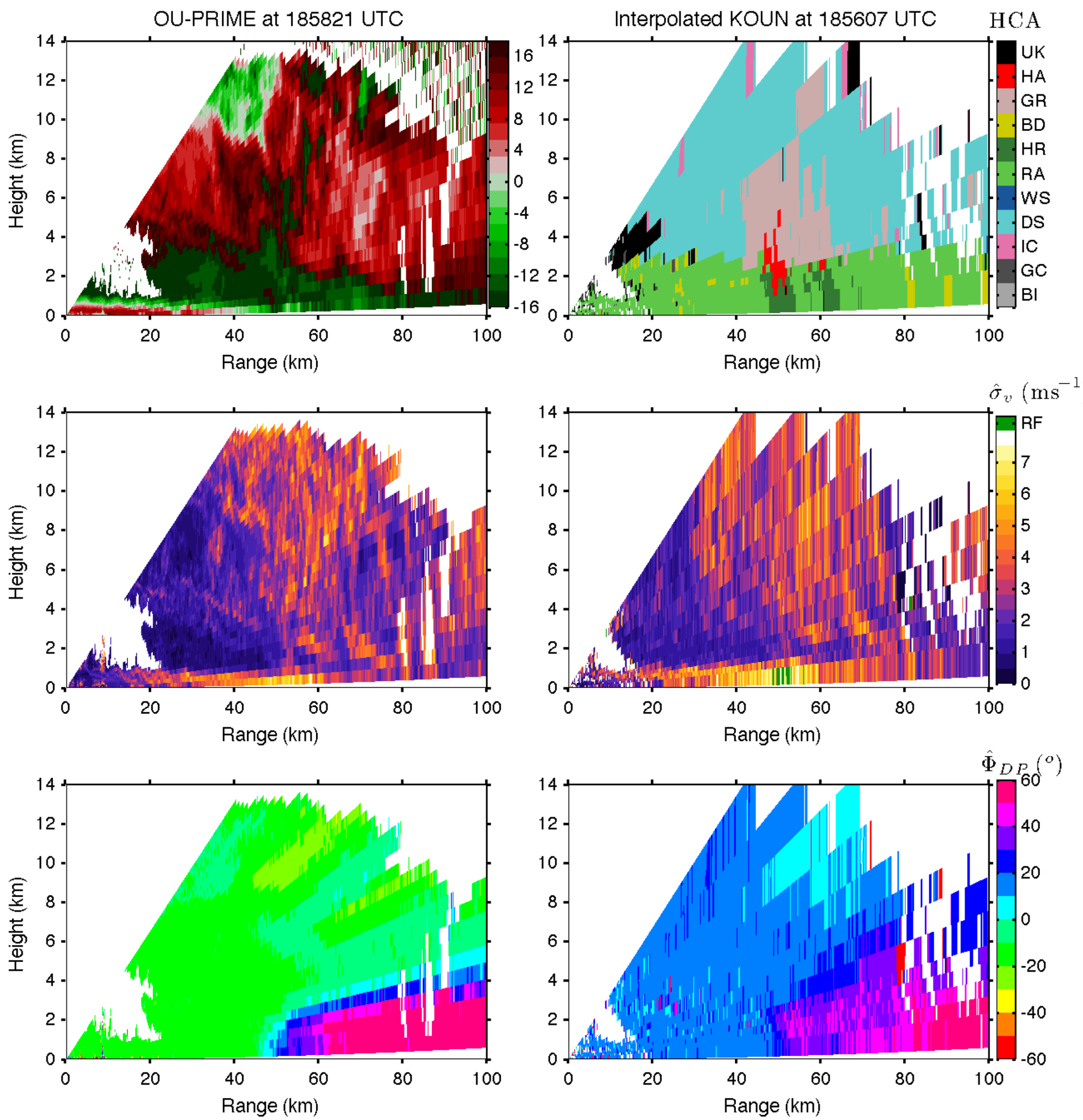

Figure 2: Similar to Fig. 1 but for radial velocity, spectrum width and differential phase from OU-PRIME RHI scan (left panels) and for HCA, spectrum width and differential phase from KOUN (right panels) at 18:56:07 UTC

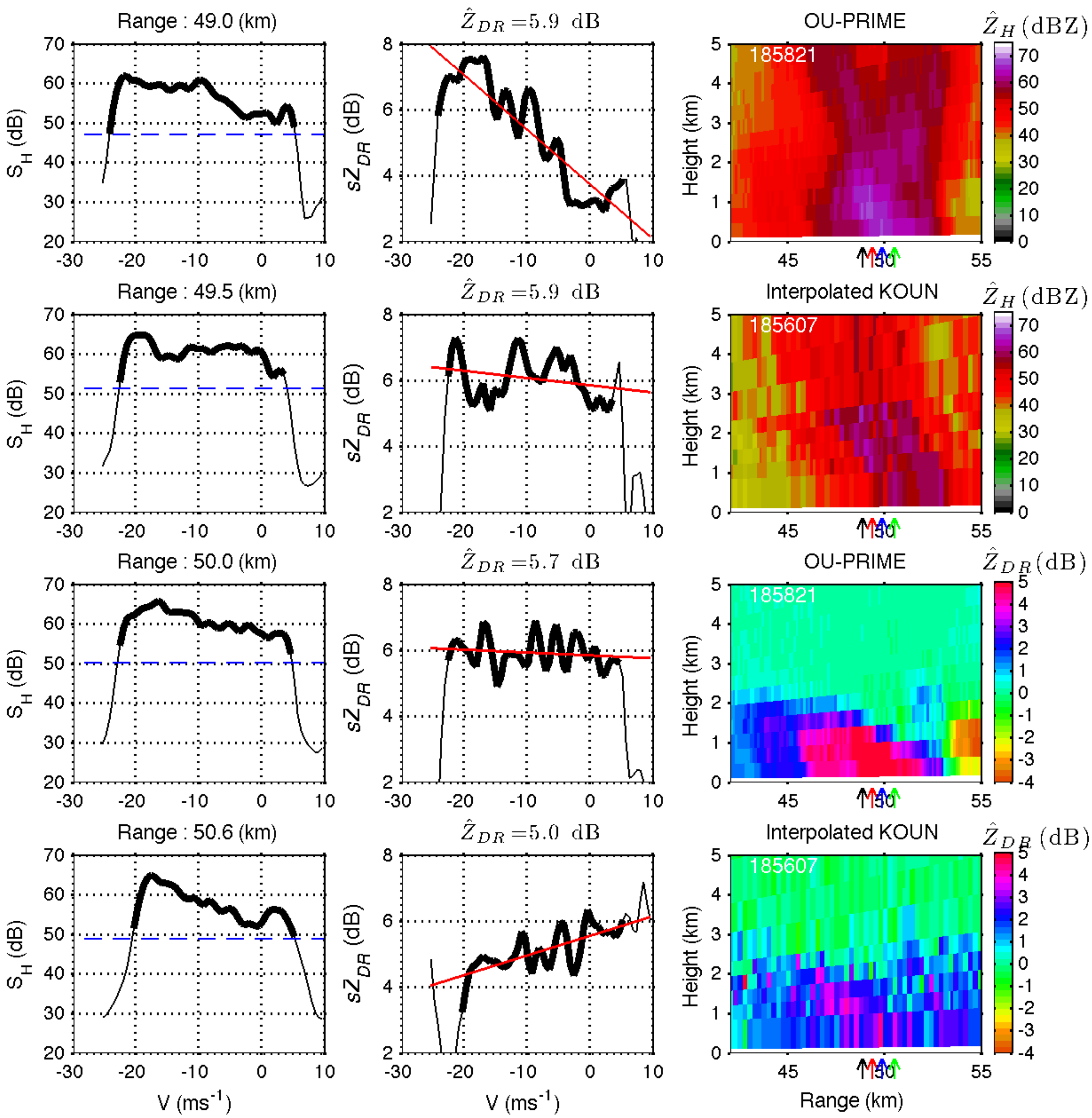

Figure 3: Spectral reflectivity, spectral differential reflectivity at selected ranges of 49, 49.5, 50 and 50.6 km from OU-PRIME. In the third column from top to bottom column, zoom-in reflectivity from OU-PRIME RHI scan at 18:58:21 UTC, zoom-in reflectivity from the interpolated KOUN at 18:56:07 UTC, zoom-in differential reflectivity from OU-PRIME and zoom-in differential reflectivity interpolated from KOUN are shown.

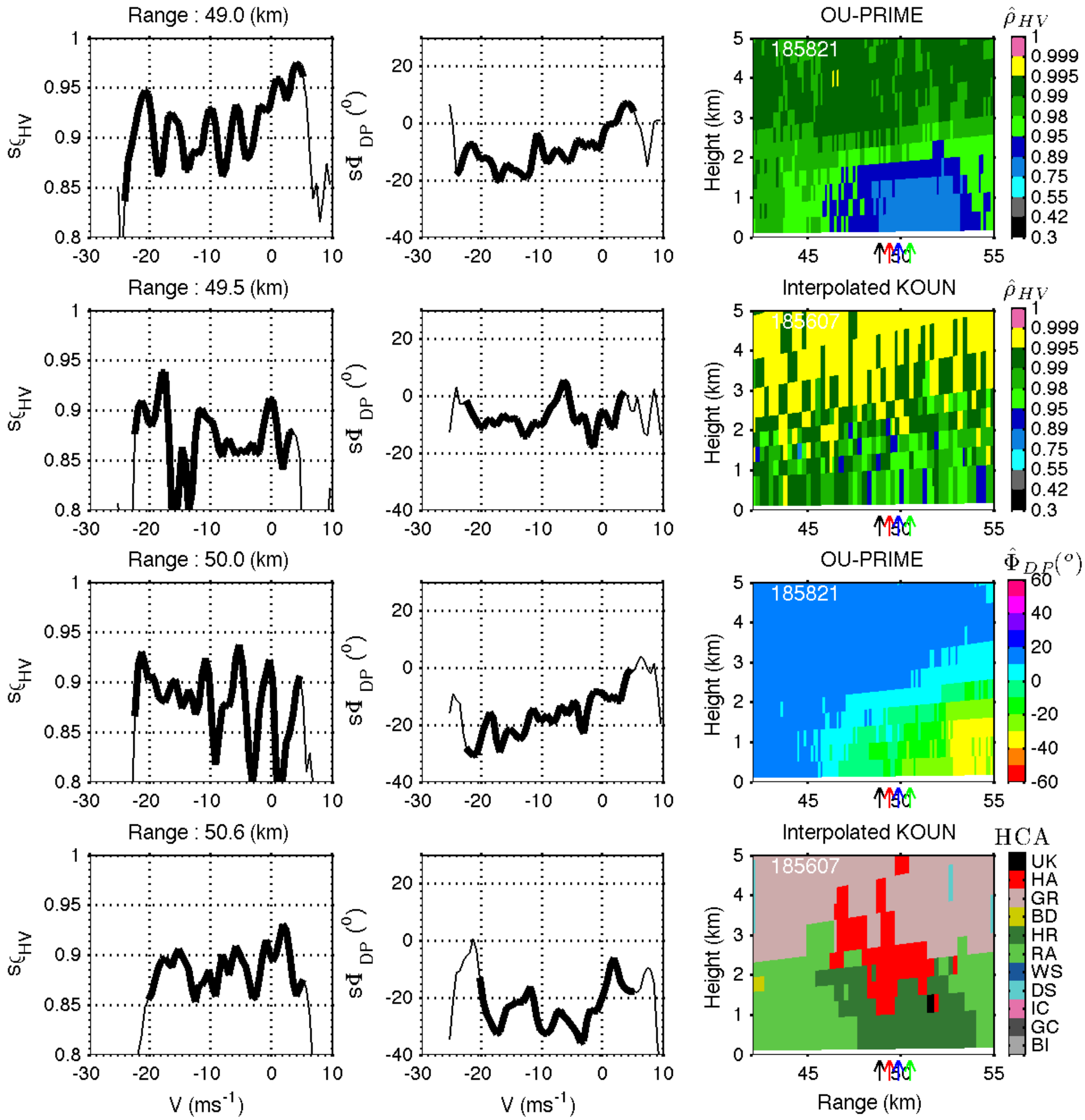

Figure 4: Spectral co-polar correlation coefficient, spectral differential phase at same selected ranges as those from Fig. 3. In the third column, zoom-in co-polar correlation coefficient from OU-PRIME RHI scan at 18:58:21 UTC, zoom-in co-polar correlation coefficient from the interpolated KOUN at 18:56:07 UTC are shown. The next two panels are the zoom-in differential phase from OU-PRIME and HCA results from interpolation at 18:56:07 UTC from KOUN.

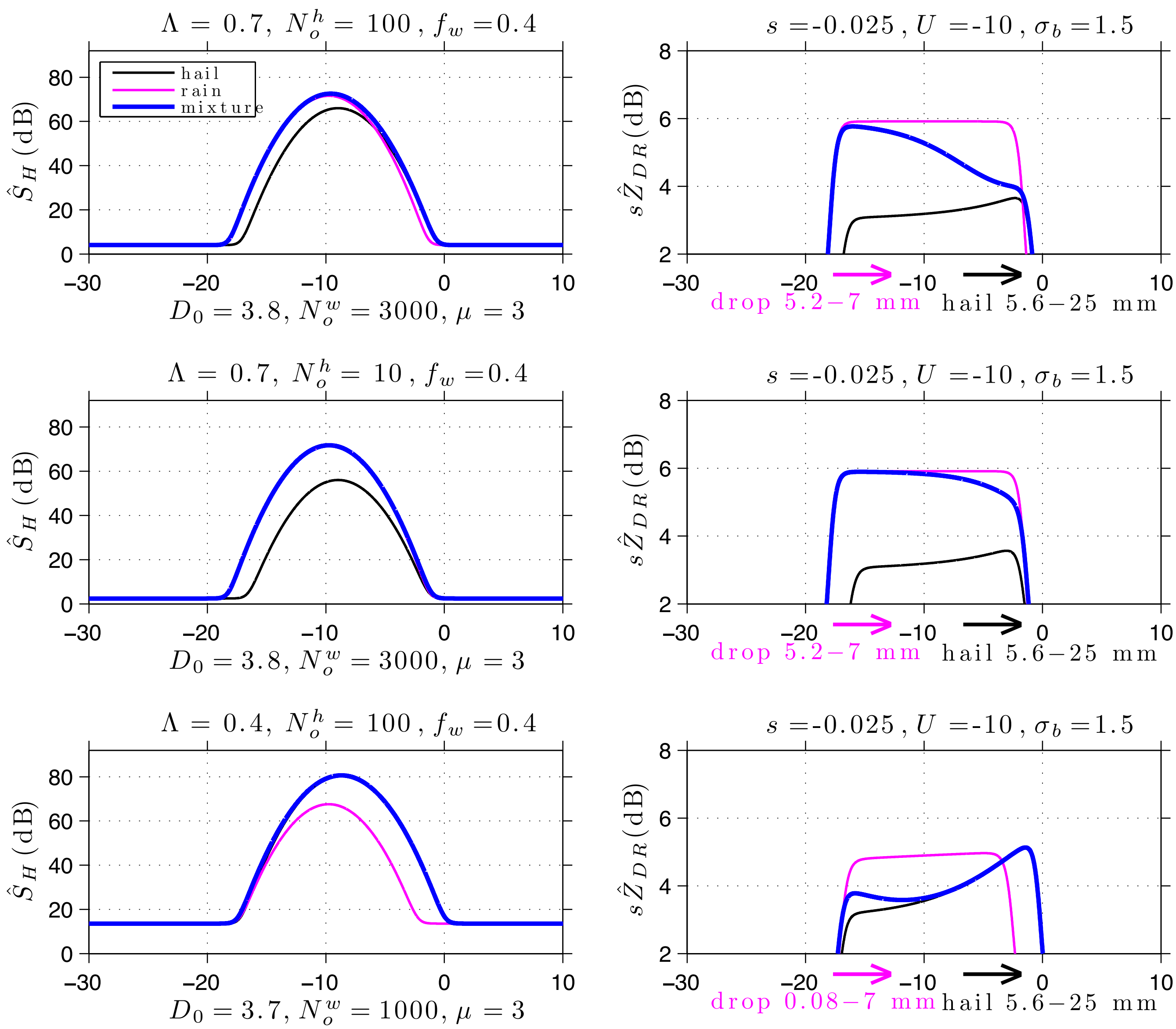

Figure 5: Simulation results that reproduce spectral polarimetric signatures observed by OU-PRIME RHI at 18:58:27 UTC